IEEE Access
Multidisciplinary ⋮ Rapid Review ⋮ Open Access Journal

Received 14 December 2022, accepted 30 December 2022, date of publication 18 January 2023, date of current version 26 January 2023.

Digital Object Identifier 10.1109/ACCESS.2023.3237909

RESEARCH ARTICLE

Performance-Based Tuning for a Model Predictive Direct Power Control in a Grid-Tied Converter With L-Filter

JEFFERSON S. COSTA[1,2], ANGELO LUNARDI[1], POLLYANA C. RIBEIRO[3], IAGO B. DA SILVA[3], DARLAN ALEXANDRIA FERNANDES[3], (Member, IEEE), AND ALFEU J. SGUAREZI FILHO[1], (Senior Member, IEEE)

[1]Center for Engineering, Modeling and Applied Social Sciences, Federal University of ABC, Santo André, São Paulo 09210-580, Brazil
[2]Department of Electrical Engineering, Federal University of Pará, Tucuruí, Pará 68455-901, Brazil
[3]Department of Renewable Energies Engineering, Federal University of Paraíba, João Pessoa, Paraíba 58051-900, Brazil

Corresponding author: Jefferson S. Costa (jeffersonsc@ufpa.br)

This work was supported in part by the Conselho Nacional de Desenvolvimento Científico e Tecnológico (CNPq) under Grant 405757/2018-2 and Grant 407867/2022-8, and in part by the Fundação de Amparo à Pesquisa do Estado de São Paulo (FAPESP) under Grant 2022/00323-3.

ABSTRACT Model predictive control (MPC) is a powerful and widely used technique to address the control challenges in power converters as the grid interface for renewable energy systems. This technique combines closed-loop control with error and control effort minimization; however, its design is challenging, and we know little about how the controller parameters affect the closed-loop performance of grid-connected voltage source converters. In this study, we applied an MPC direct power control with modulation for a grid-connected power converter with an inductive filter. For the controller design, we proposed an initial set based on the power converter's nominal setup. Then, we define the range of settings to guarantee stability by analyzing the closed-loop poles of the system. The fine-tuning to improve the performance can be identified visually using the performance maps built from simulations of the control system, simultaneously sweeping the time horizons of the predictive model and the weight factors of the cost function. Experimental results on a low-power bench demonstrate the excellent performance of the designed controller, following and even outperforming the classical proportional-integral (PI) controller and other advanced control techniques.

INDEX TERMS Direct power control, grid-connected VSC, model predictive control, MPC with PWM modulation, weight factors design.

I. INTRODUCTION

Integrating renewable energy sources (RES), such as solar PV and the wind, with the electric power system is an essential solution to reduce the dependency on high carbon emission sources, such as oil derivatives and coal, which strongly contribute to global warming [1]. The development of power converter technology has contributed to the energy transition by interfacing RES in microgrids and distributed generation [2].

The Voltage Source Converter (VSC) with a passive filter is the most common power converter topology applied as a grid interface for RES [3]. The passive filter is required to attenuate the harmonic components generated by the switched voltage and by nonlinearities such as the dead time of the VSC switches [2]. The inductive (L) filter is the more straightforward, well-established, and more reliable since it requires a minimum of sensors compared to higher order filters such as inductive-capacitive (LC) or inductive-capacitive-inductive (LCL) [4], [5]. Although higher-order filters offer advantages in size, cost, and attenuating harmonic distortions, the control system design and implementation complexity increases significantly due to the characteristic

The associate editor coordinating the review of this manuscript and approving it for publication was Qi Zhou.

resonance, which demands an active or passive method of attenuation [5], [6].

The good dynamic performance and robustness of the grid-connected VSC depend on the control technique applied; the most common include the classical PI current controller [7], [8], [9], resonant proportional control (PR) [6], nonlinear controls by sliding modes or Fuzzy interface [2], state feedback [10], and MPC [11]. The MPC combines the attributes of other advanced control techniques such as closed-loop control, error and control effort minimization, intuitive implementation for multi-variable systems, and the ability to incorporate the physical constraints [11], [12]. The main types of MPC that are gaining space on power converter applications are Deadbeat, Finite Control Set (FCS-MPC), Continuous Control Set (CCS-MPC), and Generalized Predictive Control (GPC) [2], [11], [12], [13]. The computational cost, especially when constraints are imposed, is an important limitation of MPC [14]. In addition, as a model-based technique, the MPC may lose performance due to parametric variations and large disturbances in load current or grid voltage [2], [12].

The essential operation of the MPC uses the system model to predict the future behavior of the output, a weighted cost function of the reference tracking error and control effort, and an optimization strategy to compute the control signal [15]. The CCS-MPC, also known as MPC with modulation, uses a state space matrix modeling, produces a control signal continuous in amplitude within an allowable voltage range for the VSC, and operates with a constant switching frequency [12]. The classical approach of the CCS-MPC technique is the current control [15]. Another usual approach is Direct Power Control (DPC), called MPC-DPC, which considers the active and reactive powers as state variables of the grid-connected VSC [15], [16]. The MPC-DPC is usually applied in the synchronous rotation frame for simplifying individual control of the active e reactive power [7], [16]. It can also be applied in the stationary frame, such as in [17].

In this paper, an MPC-DPC is designed in the synchronous rotation frame for a grid-connected VSC with L-filter. The primary motivation is to contribute to the energy transition by developing control systems to power converters as a grid interface for RES. The systematic design of the MPC-DPC controller is an open scientific challenge since there are various degrees of freedom, such as the time horizons in the predictive model and the cost function weight factors that affect the stability and performance of the system [18]. Because of the complexity, the empirical method is the most commonly reported for the design, as in [19].

The MPC-DPC control system must guarantee the closed-loop stability, power regulation, and quality of the energy injected into the grid. A Phase-Locked Loop (PLL) synchronizes with the grid voltage [20]. The strong grid model is adopted here for the single small-scale grid-connected VSC, where the grid is assumed as a stiff voltage source with an impedance that has a low effect on the system stability [3], [16], [21]. To reduce the degrees of freedom to only four parameters, the cost function weighting block diagonal matrices are simplified to diagonal matrices with equal terms [22]. We proposed an initial setting for the weight factors using the square of the ratio between the VSC nominal power and the grid voltage values [11].

The proposed controller tuning is based on the closed-loop poles of the MPC-DPC control system. First, the controller settings are constrained to guarantee stability and then applied to estimate the theoretical dynamic performance. Simulated results are presented to corroborate the theoretical analyses and provide a performance mapping with the simultaneous sweep of the MPC-DPC parameters, weight factors, and time horizons. These performance maps visually identify the fine-tuning of the MPC-DPC to maximize the performance in power regulation and energy quality of the grid-connected VSC. Similar analyses of the CCS-MPC parameters and the performance of the grid-connected VSC have been presented for classical current control, such as in [23] and [24]. However, we found no reports for the MPC-DPC controller. The proposed controller tuning were validated experimentally and compared to the PI-DPC control proposed in [7] using a 1 kW workbench.

II. MODEL OF THE VSC IN ROTATION FRAME *dq*

The grid-connected power converter (Fig. 1) consist of a VSC with L-filter [12], [25]. The VSC injects energy into the grid from the DC bus by modulating the voltage V_{dc} into a three-phase waveform v_i^{abc} synchronized with the grid common connection point (CCP) [26]. The full operation of the system (Fig. 1) depends on the proper drive of the VSC switches by the space vector MPC-DPC control strategy in rotation frame dq [11]. The MPC-DPC uses a predictive model, defined in section III, and a cost function of the tracking error of P_{ref} and Q_{ref}, and the control effort $\vec{u}_{dq}$ [27]. The minimization of the cost function is the key step and produces the reference signal for driving the VSC in the form $\vec{v}_i^{ref}(k) = \vec{u}_{dq}(k) + \vec{v}_{g,dq}(k)$ (Fig. 1). A space vector PWM modulator (SPWM) performs the VSC switch drive from the $\vec{v}_{i,dq}^{ref}$ signal after the conversion to the $\alpha\beta$ stationary frame [11].

The synchronization with the grid voltage is performed by a PLL, as shown in Fig. 2, a simple and robust control loop that estimates the instantaneous phase θ_g [20]. The measurement of the three-phase currents (i_g^{abc}) and voltages (v_g^{abc}) at the grid CCP are required for the operation of the control loop (Fig. 1), which are converted to the synchronous frame dq first using the Clarke transform and then using θ_g and the Parke transform [28]. In the PLL (Fig. 2), the grid voltage vector $\vec{v}_{g,dq}$ and the d-axis of the rotating frame dq are forced into synchronism at the same angle θ_g as estimated by the PI control loop, so that the Parke transform result in $v_{g,q} = 0$ and $|\vec{v}_{g,dq}| = v_{g,d}$ [20]. This strategy creates a weak coupling between the d and q components of the system variables since it allows the individual control of active power P and reactive power Q by using only the components $i_{g,d}$ and

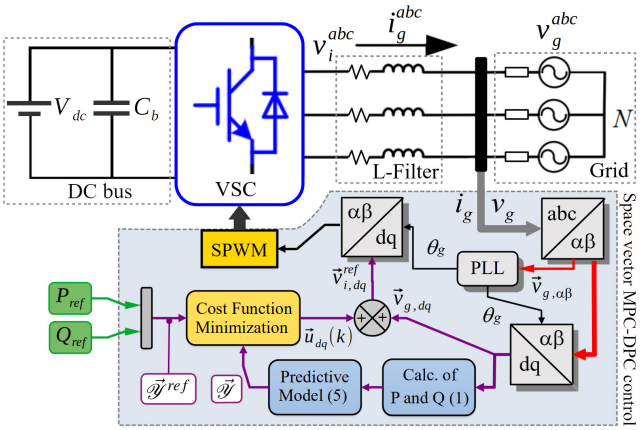

FIGURE 1. Space vector MPC-DPC strategy for the grid-connected VSC with L-filter using rotation frame *dq*.

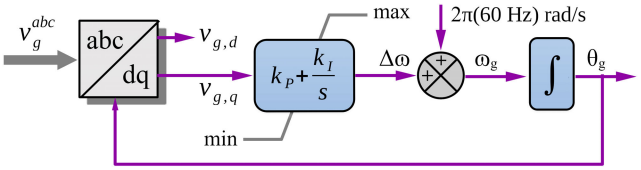

FIGURE 2. Block diagram representing the operation of the PLL.

$i_{g,q}$, respectively, as established in (1) [11].

$$P = \frac{3}{2}\Re\left\{\vec{v}_{g,dq}\,\vec{i}^{*}_{g,dq}\right\} = \frac{3}{2}v_{g,d}\,i_{g,d}$$
$$Q = \frac{3}{2}\Im\left\{\vec{v}_{g,dq}\,\vec{i}^{*}_{g,dq}\right\} = -\frac{3}{2}v_{g,d}\,i_{g,q} \tag{1}$$

The continuous-time DPC model for the VSC in Fig. 1 is given in (2), where: the sub-index d and q represent the real and imaginary components of the state variables; L_g and R_g are the inductance and the internal resistance of the filter; ω_g is the grid frequency in rad/s [19], [27]. The DPC model is obtained by considering $v_{g,d}$ constant during the short sampling time and under ideal grid operating conditions [27], and deduced from the components $i_{g,d}$ and $i_{g,q}$ in (1) replaced in the current model of the VSC with L-filter [12].

$$\begin{bmatrix}\frac{dP}{dt}\\ \frac{dQ}{dt}\end{bmatrix} = \begin{bmatrix}-\frac{R}{L} & \omega_g\\ -\omega_g & -\frac{R}{L}\end{bmatrix}\begin{bmatrix}P\\ Q\end{bmatrix} + \begin{bmatrix}\frac{3v_{g,d}}{2L} & 0\\ 0 & -\frac{3v_{g,d}}{2L}\end{bmatrix}\begin{bmatrix}v_{i,d}-v_{g,d}\\ v_{i,q}-v_{g,q}\end{bmatrix} \tag{2}$$

The discrete DPC model in (3) is obtained approximating the power derivatives in (2) by a zero-order-hold (ZOH) [22]. Discretization errors can be neglected effectively due to the high ratio between the sampling frequency and the operating frequency of the system [29]. In (3) $\vec{u}_{dq} = \vec{v}_{i,dq} - \vec{v}_{g,dq}$ is an auxiliary variable representing the difference between the VSC and grid voltages, and C_d is an identity matrix 2×2.

The brackets in (3) identify the compact model terms in (4).

$$\overbrace{\begin{bmatrix}P(k+1)\\ Q(k+1)\end{bmatrix}}^{\vec{x}(k+1)} = \overbrace{\begin{bmatrix}1-\frac{RT_s}{L} & \omega_g T_s\\ -\omega_g T_s & 1-\frac{RT_s}{L}\end{bmatrix}}^{A_d}\overbrace{\begin{bmatrix}P(k)\\ Q(k)\end{bmatrix}}^{\vec{x}(k)} + \underbrace{\begin{bmatrix}\frac{3v_{g,d}T_s}{2L} & 0\\ 0 & -\frac{3v_{g,d}T_s}{2L}\end{bmatrix}}_{B_d}\underbrace{\begin{bmatrix}v_{i,d}(k)-v_{g,d}(k)\\ v_{i,q}(k)-v_{g,q}(k)\end{bmatrix}}_{\vec{u}_{dq}(k)} \tag{3}$$

$$\vec{x}\,(k+1) = A_d\vec{x}\,(k) + B_d\vec{u}_{dq}\,(k)$$
$$\vec{y}\,(k+1) = C_d\vec{x}\,(k+1) \tag{4}$$

III. MPC-DPC CONTROL FOR GRID-CONNECTED VSC

The predictive model in the MPC strategy (Fig. 1) uses the DPC model in (4) to predict the future behavior of the power injected into the grid up to the sliding horizon n_y [19], [27]. Successive applications of (4) form the predictive model in (5), where: $\vec{\mathcal{Y}} \in \Re^{n_y\times 2}$ is the prediction vector of the system output defined in (6); $\vec{x}\,(k)$ are the actual measurements of the states variables; $U \in \Re^{2\,n_u\times 1}$ is the prediction vector of the control signal up to the horizon n_u defined in (7); Ψ is the predictive state matrix defined in (8); and $\mathcal{M}$ is the input matrix defined in (9).

$$\vec{\mathcal{Y}} = \Psi\,\vec{x}\,(k) + \mathcal{M}\,U \tag{5}$$
$$\vec{\mathcal{Y}} = \left[\vec{y}(k+1)\;\vec{y}\,(k+2)\;\cdots\;\vec{y}\,(k+n_y)\right]^{\top} \tag{6}$$
$$U = \left[\vec{u}_{dq}(k)\;\;\vec{u}_{dq}(k+1)\;\;\cdots\;\;\vec{u}_{dq}(k+n_u-1)\right]^{\top} \tag{7}$$
$$\Psi = \left[C_dA_d\;C_dA_d^2\;C_dA_d^3\;\cdots\;C_dA_d^{n_y}\right]^{\top} \tag{8}$$
$$\mathcal{M} = \begin{bmatrix} C_dB_d & 0 & \cdots & 0\\ C_dA_dB_d & C_dB_d & \cdots & 0\\ C_dA_d^2B_d & C_dA_dB_d & \cdots & 0\\ \vdots & \vdots & \ddots & \vdots\\ C_dA_d^{n_y-1}B_d & C_dA_d^{n_y-2}2B_d & \cdots & C_dB_d\end{bmatrix} \tag{9}$$

A. COST FUNCTION

The quadratic cost function in (10) uses the predictions of the reference $\vec{\mathcal{Y}}^{ref} \in \Re^{2n_y\times 1}$, the system output (3) and the control signal (7) [27]. The terms Γ_y and Γ_u in (10) are diagonal weighting matrices of the tracking error and the control effort, respectively.

$$\mathcal{J} = \left(\vec{\mathcal{Y}}_{ref} - \vec{\mathcal{Y}}\right)^{\top}\Gamma_y\left(\vec{\mathcal{Y}}_{ref} - \vec{\mathcal{Y}}\right) + U^{\top}\Gamma_u U \tag{10}$$

The vector $\vec{\mathcal{Y}}^{ref}$ is defined from the reference signal $\vec{y}^{ref}\,(k) = \vec{i}^{ref}_{g,dq}(k)$ repeated n_y times in (11) [12]. In this sense, the grid voltage is considered constant within the prediction horizon n_y, a strategy known as persistent MPC [30] and consistent with DC values in the dq synchronous frame for any n_y. In [19], this strategy is used to formulate the CCS-MPC in the $\alpha\beta$ stationary frame, but the approximation is restricted to short time horizons [11]. The weight factors $\Gamma_y \in Re^{2n_y\times 2\,n_y}$ and $\Gamma_u \in Re^{2n_u\times 2\,n_u}$ are positive definite block diagonal matrices [12]. The cost function weighting block

diagonal matrices are simplified to diagonal matrices with equal terms, as shown in (12) and (13), to reduce the degrees of freedom associated with the MPC-DPC controller [22]. Thus, the critical parameters to the performance of the MPC-DPC are reduced to four: γ_y, γ_u, n_y, and n_u.

$$\vec{\mathcal{Y}}^{ref}_{[2n_y\times 1]} = \left[1\ 1\ 1\ \cdots\ 1\right]^{\top} \vec{y}^{\,ref}(k) \tag{11}$$

$$\Gamma_{y\,[2n_y\times 2n_y]} = \gamma_y\, diag(\left[1\ 1\ 1\ \cdots\ 1\right]) \tag{12}$$

$$\Gamma_{u\,[2n_u\times 2n_u]} = \gamma_u\, diag(\left[1\ 1\ 1\ \cdots\ 1\right]) \tag{13}$$

B. MINIMIZATION OF THE COST FUNCTION

In the MPC strategy applied in this paper, we do not assume constraints for the system variables, allowing us to obtain an analytical solution for minimizing the cost function (10) by solving $\partial\mathcal{J}/\partial U = 0$ [15]. The solution U presented in (14) is a control signal prediction vector, as defined in (7), where the first element is the control signal for the recent horizon $\vec{u}_{dq}(k)$ to be applied to the system [18]. The control signal $\vec{u}_{dq}(k)$ can be obtained from (14) in the form $\vec{u}_{dq}(k) = \mathcal{W}\,U$, where $\mathcal{W} = \left[I_{2\times 2}\ \mathbf{0}\ \cdots\ \mathbf{0}\right]_{[2\times(2n_u+2)]}$.

$$U = \left(\mathcal{M}^{\top}\Gamma_y\mathcal{M} - \Gamma_u\right)^{-1}\mathcal{M}^{\top}\Gamma_y\left[\vec{\mathcal{Y}}_{ref} - \Psi\,\bar{x}\,(k)\right] \tag{14}$$

A more compressible way to define the control signal $\vec{u}_{dq}(k)$ is presented in (15), where $\mathcal{K} = \mathcal{W}\left(\mathcal{M}^{\top}\Gamma_y\mathcal{M} - \Gamma_u\right)^{-1}\mathcal{M}^{\top}\Gamma_y$ is a constant matrix and independent of the measurements of the system variables, so can be calculated external to the real-time control loop [18]. The computational load of (15) is similar to simple state feedback [31], but implements the error and control effort minimization at each time instant when the reference is updated and new measurements of the state variables are available [15].

$$\vec{u}_{dq}(k) = \mathcal{K}\left[\vec{\mathcal{Y}}_{ref} - \Psi\,\bar{x}\,(k)\right] \tag{15}$$

IV. DESIGNING OF THE CCS-MPC CONTROLLER

A. STABILITY ANALYSIS

The design of the CCS-MPC controller is complex because it is necessary to adjust multiple parameters that sensitively affect the stability and closed-loop performance [23]. The classical root-locus stability criteria for discrete linear systems state that all closed-loop poles must be inside the unit circle in the z-plane to ensure stability [32]. We use this concept to impose constraints on the CCS-MPC controller parameters. According to [33], the closed-loop poles of the CCS-MPC controller are the eigenvalues given by (16), which can be deduced by substituting the control law (15) into the discrete model in (4). The configuration of the grid-connected VSC used in this paper is summarized in Table 1 [22].

$$\left|A_d - B_d\mathcal{K}\Psi - zI\right| = 0 \tag{16}$$

Fig. 3 shows with "x" markers the closed-loop poles (16) for a finite set of the parameters γ_y, γ_u, n_y, and n_u. Note that the poles move from the right boundary of the unit circle to the center (Fig. 3) as γ_u decreases with constant

Algorithm 1 MPC-DPC Algoritm

Result: VSC switch drive: optimal duty cycle.
Load the system parameters: R, L, V_{ab}, f_g, V_{dc}, f_{sw}, γ_y, γ_u, n_y, n_u;
while *MPC-DPC active* **do**
  Acquisition of the 3-phase $\vec{i}_{g,abc}(k)$ and $\vec{v}_{g,abc}(k)$;
  Apply Clark transform: $\vec{i}_{g,\alpha\beta}(k)$ and $\vec{v}_{g,\alpha\beta}(k)$;
  Active PLL for grid synchronization: $\theta_g(k)$;
  Apply Park transform: $\vec{i}_{g,dq}(k)$ and $\vec{v}_{g,dq}(k)$;
  Apply (1): $\vec{x}(k) = [P(k),\ Q(k)]$;
  Build the system model (4): A_d, B_d, and C_d;
  Build the predictive model (5): Ψ, $\mathcal{M}$ and $\mathcal{Y}_{ref}$;
  Build the cost function $\mathcal{J}$ (10);
  Minimize $\mathcal{J}$ using (15): $\vec{u}_{dq}(k)$;
  $\vec{v}_{i,dq}(k) = \vec{u}_{dq}(k) + \vec{v}_{g,dq}(k)$;
  Apply inverse Park transform: $\vec{v}_{i,\alpha\beta}(k)$);
  Apply $\vec{v}_{i,\alpha\beta}(k)$) to the SPWM modulator;
  Drive the VSC switches;
end

TABLE 1. Setup of the grid-connected VSC.

Used in	Parameter	Value
Grid-connected VSC	P nominal	750 W
	Q nominal	300 var
	Nominal power	1 kVA
	V_{ab}	~190 V_p
	f_g	60 Hz
	V_{dc}	300 V
	f_{sw}	20 kHz
L-filter	L	13.2 mH
	R	0.1 Ω

γ_y, improving the transitory response such as decreasing the settling time t_s [32]. The values of t_s in Fig. 3 were calculated by approximating with an ideal second order system, considering the 2% settling criteria [32]. According to [24], the γ_y setting can be arbitrary since the cost function minimum point is independent of the absolute values of γ_y and γ_u, but rather the ratio between them. Thus, the closed-loop dynamic response improves as the ratio γ_u/γ_y decreases, either reducing γ_y with fixed γ_y (Fig. 3) or increasing γ_y with fixed γ_u.

The proposed initial setting ($\gamma_y = 10^3$, $\gamma_u = 10^5$) or $\gamma_u/\gamma_y = 10^2$ is approximately the square of the ratio between the nominal values of the VSC power (S_n = 1000 VA) and the grid voltage (v_g = 110 V):

$$\frac{S_n^2}{v_g^2} = \frac{1000^2}{110^2} = 82.64 \approx 1\times 10^2, \tag{17}$$

which, in the worst case, causes approximately equal contribution of the cost function the weighted terms tracking error and control effort [11]. This tuning strategy is similar to the case of the FSC-MPC applied to the torque and flux control of the Doubly Fed Induction Generator

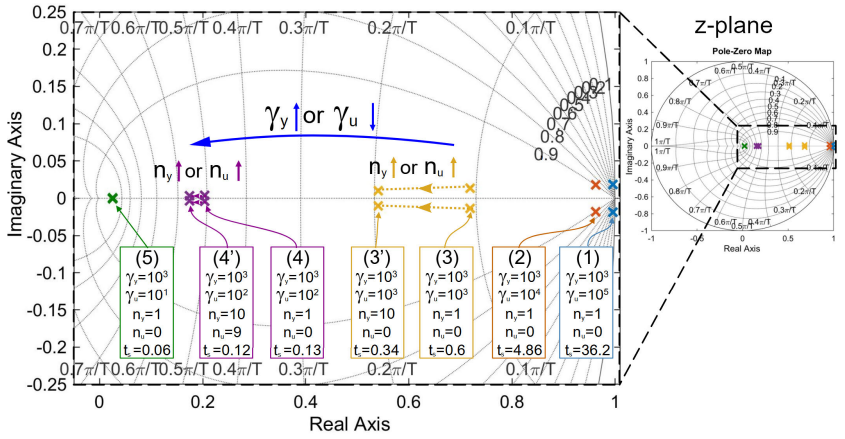

FIGURE 3. Highlighting the unit circle in the z-plane for the root locus of some MPC-DPC controller settings. Values of t_s in milliseconds.

(DFIG) [11], [28]. The initial setting (1) (Fig. 3) produces poles near the unit circle boundary, so it is defined as the reference for the stability. Notice finally in Fig. 3 that increasing the horizons n_y and n_u also moves the poles toward the center of the unit circle, such as the settings (3) and (4) moves when the horizons change from $n_y = 1$ and $n_u = 0$ to $n_y = 10$ and $n_u = 9$.

B. CONTROLLER TUNING

This section presents the closed-loop performance mapping for tuning the CCS-MPC DPC controller from the ranges where stability is guaranteed (section IV-A). This analysis was performed in SimPowerSystems toolbox of Matlab/Simulink®, using the settling time and integral square error (ISE), as defined in (18) [34], to analyze the transient and steady-state power regulation dynamic [35]. In (18) $\vec{e} = \left[P - P_{ref}, Q - Q_{ref}\right]^\top$ is the error vector of active and reactive power reference tracking. The total harmonic distortion (THD) of the current injected into the grid (Fig. 1) was used to evaluate the energy quality, which should not be greater than 5% as recommended by the IEEE 1547.2-2008 standard [36].

$$ISE = \|\vec{e}\,(t)\|_2 = \sqrt{\int_0^\infty |\vec{e}\,(\tau)|^2 \; d\tau} \tag{18}$$

As a starting point for tuning the MPC-DPC controller, we considered here only the setting (3) or higher (Fig. 3), i.e., setting $\gamma_u/\gamma_y \leq 10^0$. Since the theoretically dynamic response (t_s) for setting (2) is much slower than the benchmark of other advanced control techniques, for example, in [22] where the settling time is approximately 2 ms. To evaluate the simulated performance of the control system, the power regulation curves and the current injected into the grid were used, as shown in Fig. 4 and 5 for the setting (3). In this case, the ISE performance in power regulation is 10.42 dB (Fig. 4) and, through the spectral analysis of the grid side current $i_{g,a}$ (Fig. 5b), the ISE performance in energy

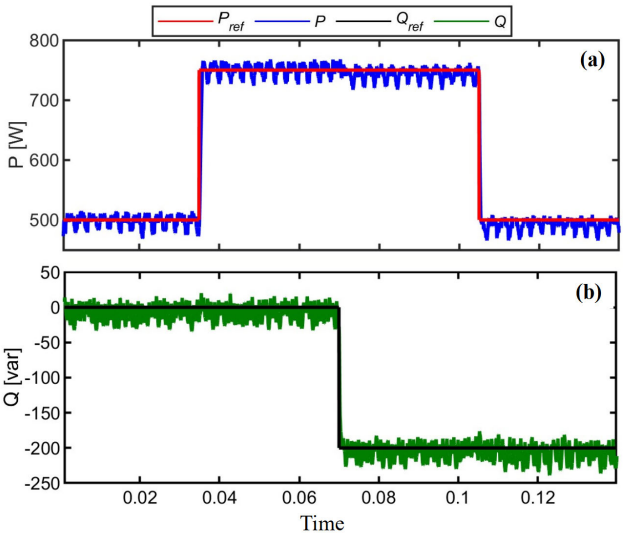

FIGURE 4. Simulated (a) active and (b) reactive power regulation for the grid-connected VSC using the MPC-DPC setting (3) (Fig. 3).

quality is 2.17%. To compare the performance of MPC-DPC settings (3), (4), and (5), Fig. 6a shows the transient regime for the simulated active power curves, and Fig. 6b presents the ISE and THD performances.

Notice in Fig. 6a that the power regulation transitory performance improves from setting (3) to (4) and from (5) to (5), i.e., reducing the γ_u/γ_y ratio, in agreement with the theoretical trend pointed out by the t_s values shown in Fig. 3. It is important to emphasize that although the theoretical t_s is an excellent indication to design the dynamic response, deviations from the plant are expected, even in simulation, due to limitations and unmodeled dynamics of the power converter, as reported in [37]. The simulated performance in power regulation and energy quality also improves with the reduction of the γ_u/γ_y ratio, as shown in Fig. 6b. The THD is a measure relative to the fundamental component of $i_{g,a}$, so a reduction in power quality is expected for power setups lower

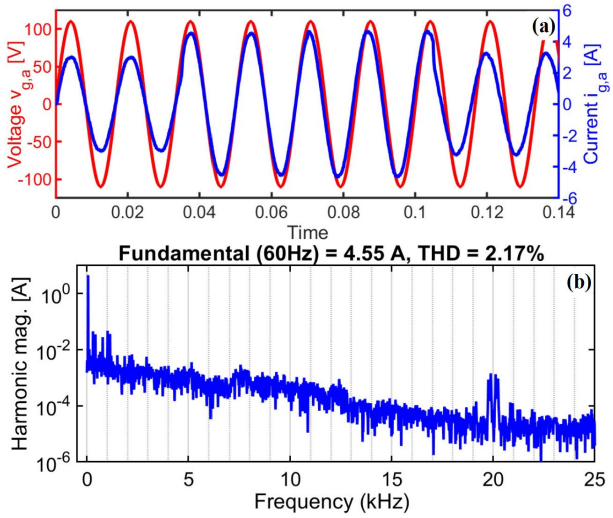

FIGURE 5. (a) Comparison of the current $i_{g,a}$ and the voltage $v_{g,a}$ at the grid CCP using the MPC-DPC setting (3), in the same time window in Fig. 4; (b) Spectral components of $i_{g,a}$ for $P_{ref} = 750$ W and $Q_{ref} = 0$ var.

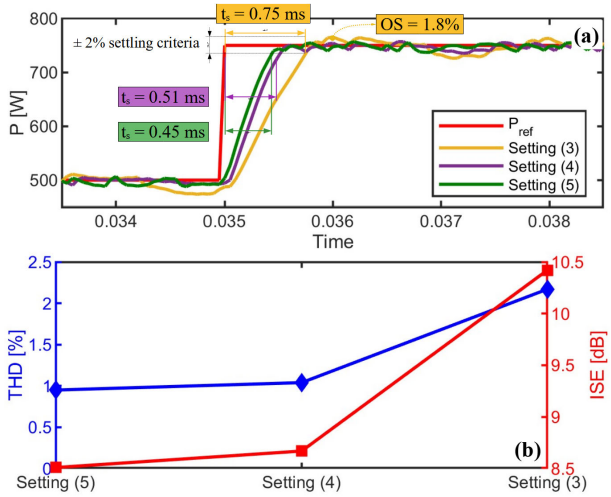

FIGURE 6. Comparison of simulated performance of the MPC-DPC settings (3), (4), and (5): (a) Active power curves in the transient regime, the inserts highlight the settling time; (b) ISE power regulation and THD energy quality.

than the nominal value of the VSC [36]. The simulated results of the MPC-DPC control system with setting (5) indicate that the minimum power set up to meet the 5% benchmark in energy quality is 20% of the nominal power (e.g., $P_{ref} = 200$ W and $Q_{ref} = 0$ var). The following subsections present further simulated studies on the effect of MPC-DPC controlling parameters on the closed-loop performance of the grid-connected VSC system.

C. EFFECT OF PREDICTION AND CONTROL HORIZONS

The influence of n_y and n_u on ISE and THD performance is evaluated in this section, for the fixed setting of the cost function gains $\gamma_y = 10^3$ and $\gamma_u = 10^3$ or $\gamma_u/\gamma_y = 10^0$ (setting (3) of Fig. 3). We evaluated the VSC performance metrics for pairs of n_y and n_u, and Fig. 7 presents the results as color maps. Note in Fig. 7 that simultaneously increasing n_y and n_u improves both ISE and THD performance (blue regions) of the grid-connected VSC, which is due to improved prediction of the system variables [11]. To avoid the low performance regions in both Fig. 7a and Fig. 7b (regions in red), an appropriate choice for time horizons might be $n_y > 1$ and $n_u = n_y - 1$.

D. EFFECT OF COST FUNCTION WEIGHT FACTORS

Considering the lower time horizons for the MPC-DPC, $n_y = 1$ and $n_u = 0$, we evaluate in Fig. 8 the effect of γ_y and γ_y on the closed-loop performance of the VSC. Only results in the region above the line $\gamma_u/\gamma_y = 10^0$ are considered stable. The results (Fig. 8) show that γ_y and γ_y affect the performance of the VSC very significantly, as expected by the dominance in the closed-loop pole placement (Fig. 7). Note in Fig. 8 that the contour lines of the THD and ISE follow the trend of the lines with the constant γ_u/γ_y ratio, evidence that the performance of CCS-MPC is independent of the absolute values of γ_y and γ_y, as mentioned earlier [24]. Figure 8 also shows that the setting $\gamma_u/\gamma_y = 10^0$ can guarantee energy quality performance better than the 5% benchmark. In contrast, an improper choice (e.g. $\gamma_u/\gamma_y = 10^1$) can worsen the power regulation performance by dozens of times compared to $\gamma_u/\gamma_y = 10^0$.

E. GLOBAL PERFORMANCE MAP FOR THE CCS-MPC PARAMETERS

This section evaluates the simultaneous effects of the time horizon and weight factors on the closed-loop performance of the DPC CCS-MPC controller, an analysis for which no report has been found in the literature using the synchronous rotating frame [23], [24]. The global performance map in Fig. 9 depends on n_y and $\gamma_u/\gamma_y = c$, where c is a constant value, while the other controller parameters are set in the form: $n_u = n_y - 1$, $\gamma_y = 10^3$ and $\gamma_u = c\gamma_y$.

The results in Fig. 9 show that the reduction of the weight factor ratio rules the tuning of the DPC controller, whereas the time horizons only significantly affect the ISE and THD when n_y is small ($n_y < 5$) or close to the line $\gamma_u/\gamma_y = 10^0$. The results suggest that the proper choice of the γ_u/γ_y ratio (vertical grid lines in Fig. 9) can guarantee good closed-loop performance for any time horizon. For example, the performance for the setting (5) $ISE = 8.51$ dB and $THD = 0.95\%$ in Fig. 9 change little with n_y.

V. EXPERIMENTAL VALIDATION OF THE CCS-MPC DPC TUNING

We use the experimental 3-phase bench presented in Fig. 10 to obtain the results presented in this paper. The main components are an electronic board for the conditioning of the three-phase voltage and current; a DSP Texas Instruments model TMS320F28335 to run all the control algorithms; a 1 kVA/500 Vdc/230 Vac power converter; a 13.5 mH/5 A

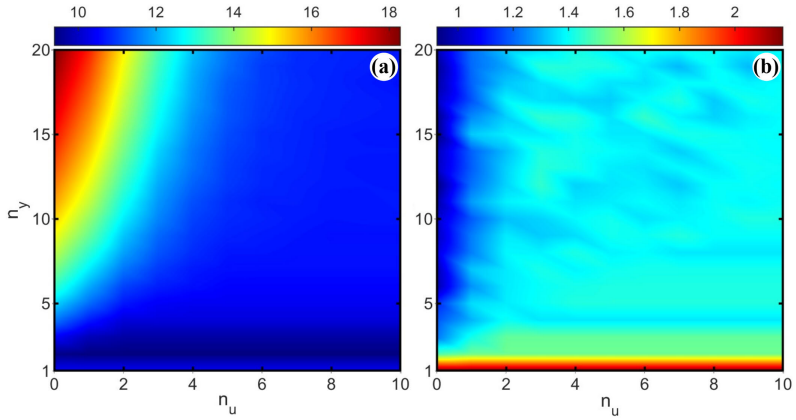

FIGURE 7. Performance map of the VSC for n_y and n_u: (a) ISE; and (b) THD.

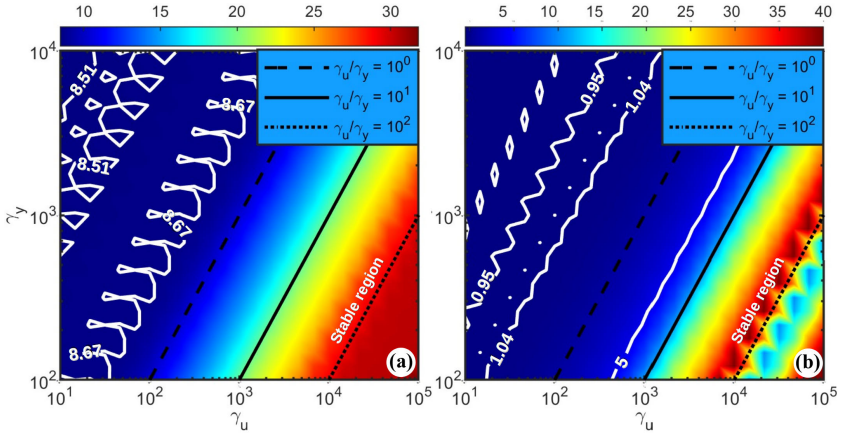

FIGURE 8. Performance map of the VSC for γ_y and γ_u: (a) ISE and (b) THD, where the contour white lines highlight the performances for the setting (4) and (5).

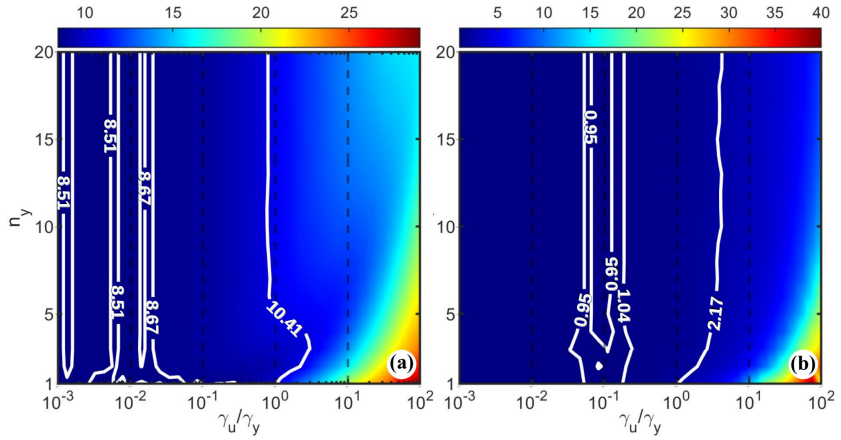

FIGURE 9. Global performance map for the CCS-MPC parameters: (a) ISE and (b) THD. In the contour white lines, the performance is equal to the setting (3), (4), and (5).

inductive bank (L filter); and an AC programmable power supply model SUPPLIER FCATHQ 4500VA/380V/500Hz to emulate the power grid [22]. The setup of the experiment grid-connected VSC is the same presented in Table 1.

The experimental validation of the proposed MPC-DPC settings starts by evaluating the performance of the settings (3), (4), and (5) shown in Fig. 3. Fig. 11 and Fig. 12 show the experimental results for the MPC-DPC settings $\gamma_u/\gamma_y = 10^0$

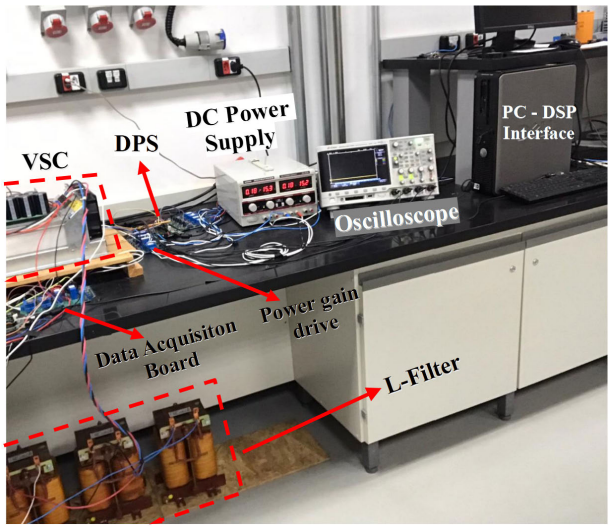

FIGURE 10. Low power experimental bench of the grid-connected VSC used for experimental validation.

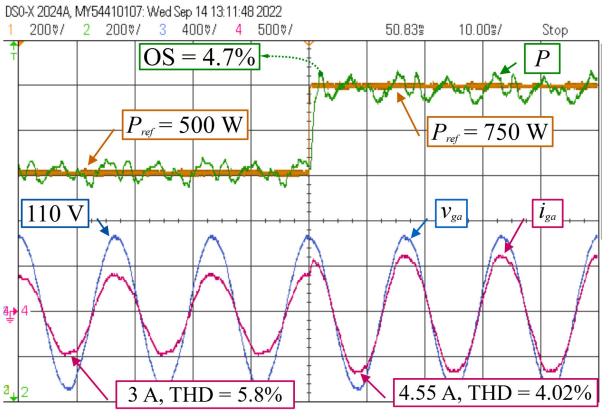

FIGURE 11. Experimental power regulation and energy quality for MPC-DPC setting (3): $\gamma_u/\gamma_y = 10^0$, $n_y = 1$, and $n_u = 0$.

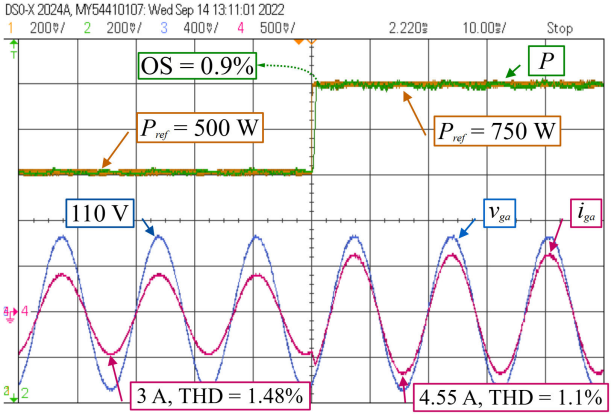

FIGURE 12. Experimental power regulation and energy quality for MPC-DPC setting (4): $\gamma_u/\gamma_y = 10^{-1}$, $n_y = 1$, and $n_u = 0$.

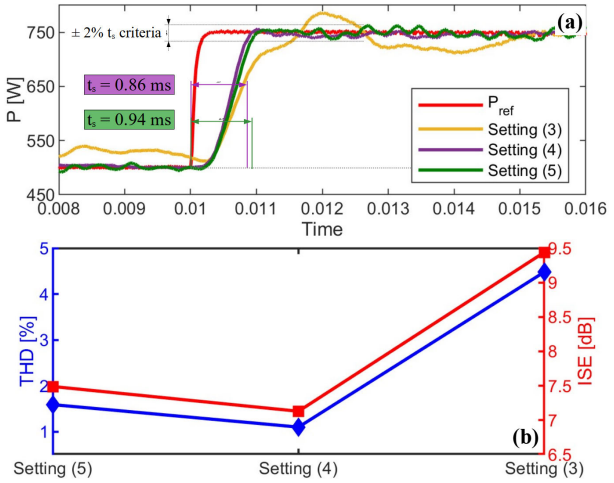

FIGURE 13. Comparison of experimental performance of the MPC-DPC settings (3), (4), and (5): (a) Active power curves in the transient regime, the inserts highlight the settling time; (b) ISE power regulation and THD energy quality.

and $\gamma_u/\gamma_y = 10^{-1}$, respectively, with the same times horizons $n_y = 1$ and $n_u = 0$. These results show an improvement of all closed-loop performance parameters from setting (3) to (4), both in transient and steady-state, as predicted in the theoretical analyses in section IV and simulated in section IV-E. Fig. 13 compares the transient of the power curves and the ISE and THD performance for the three settings (3), (4), and (5). Notice in Fig. 13 that the best experimental performance occurs in setting (4) instead of setting (5), as predicted in the theoretical and simulated analyses. This effect may be associated with the physical limits of the VSC power source [27]. Minimal values for γ_u/γ_y reduce the penalty of the control effort in the cost function, and in the limit, $\gamma_u/\gamma_y \to 0$ would require infinite energy from the VSC, which is impractical.

An important remark about the experimental performance for setting (e) is the THD = 1.1% very close to the value estimated in simulation (1.04% in Fig.6). In addition, the transient performance $t_s = 0.86$ ms is compatible and even superior to the experimental performance reported for the VSC with L-filter [22], [38] To experimentally validate the effect of the time horizon on the MPC-DPC setting, Fig. 14 compares the transient of the power curves and the ISE and THD performance for the same γ_u/γ_y values for settings (3), (4) and (5), with time horizons $n_y = 10$, and $n_u = 9$.

Notice in Fig. 14 that increasing the time horizons in the MPC-DPC produced a very close performance for the three settings (3), (4), and (5). A significant performance improvement is noted for setting (3) with $n_y = 10$, whereas in setting (5), the performance does not change with increasing n_y and n_u, precisely as predicted in the simulated analyses in section IV-E. As well as for the settings with $n_y = 10$ and $n_u = 9$ (Fig. 13), the ISE and THD performances of the settings in Fig. 14 also degrade from setting (4) to (5), this practice imposes the minimum threshold $\gamma_u/\gamma_y > 10^{-1}$ for the tuning of the MPC-DPC controller due to physical

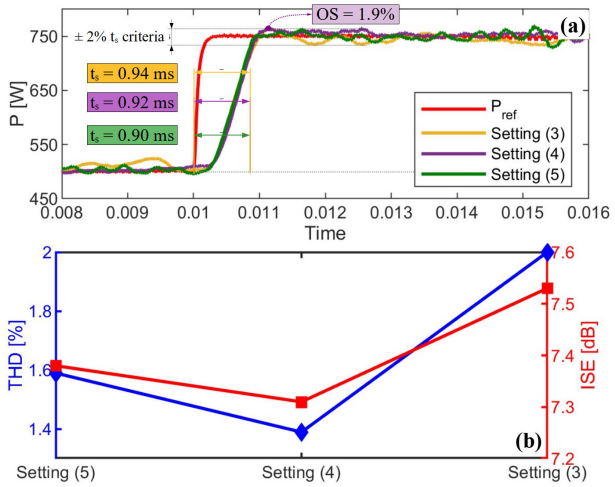

FIGURE 14. Experimental performance of the settings (3), (4), and (5) with time horizons $n_y = 10$, and $n_u = 9$: (a) Active power curves in the transient regime, the inserts highlight the settling time; (b) ISE power regulation and THD energy quality.

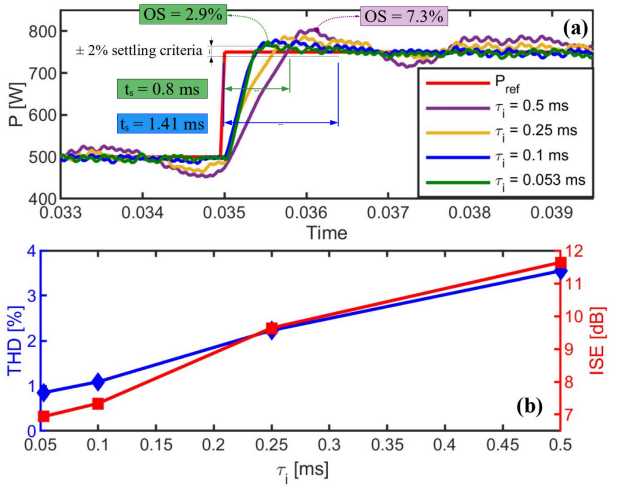

FIGURE 15. Simulated performance for the PI-DPC control of the grid-connected VSC: (a) transient response of ISE power regulation and THD performance for different PI controller settings from the indicated τ_i parameter.

TABLE 2. PI tuning from the Yasdani's method [39].

PI Param.	Tuning Proposal [39]	Discrete DPC Customization [7]
k_p	L_g/τ_i	$L_g/\tau_i \cdot (2/3V_g)^*$
k_i	R_g/τ_i	$T_s R_g/\tau_i$

* Current to power conversion using (1).

TABLE 3. Comparison between the best fit MPC-DPC and the PI DPC.

	t_s	Overshoot	THD	ISE	f_{sw}
MPC-DPC	0.86 ms	0.93%	1.1%	7.13 dB	20 kHz
PI-DPC	1.72 ms	3.99%	1.38%	7.51 dB	20 kHz

limitations of the VSC power supply [27]. Thus, the results in Fig. 14 corroborate the best experimental performance for the setting (4): $\gamma_u/\gamma_y = 10^{-1}$, $n_y = 1$ and $n_u = 0$.

A. PERFORMANCE COMPARISON WITH CLASSICAL CONTROL TECHNIQUES

This section compares the performance of the MPC-DPC controller designed in this paper with the PI DPC controller in rotation frame dq as described in [7]. The PI DPC control of the grid-connected VSC uses a PWM modulation, and it is mathematically equivalent to the classical PI current control through the gain in (1) [7]. We design the PI DPC using the well-established method proposed by [39] for dq current control of the grid-connected VSC with L-filter, which proposes the gain k_p and k_i from the parameter τ_i as shown in Table 2. Table 2 also shows the customization used here in the PI gain formulation for the discrete case of direct power control [7]. The parameter τ_i is the time constant of the approximation, by a first-order model, of the closed-loop dynamics of the plant+compensator system and should be chosen small for a fast response but large enough to ensure a closed-loop bandwidth $(1/\tau_i)$ smaller than the PWM switching frequency [39]. In this case, to conform to this rule, the PI controller bandwidth should not exceed the sampling frequency of 20 kHz. According to [39], an initial setting can be 10 times smaller bandwidth, that is, $\tau_i = 10/f_{sw} = 0.5$ ms for a $f_{sw} = 20$ kHz PWM modulator.

The tuning of the τ_i parameter was based on simulated results (Fig. 15) for the PI-DPC control of the grid-connected VSC, using the SimPowerSystems toolbox of Matlab/Simulink®. Fig. 15a shows the simulated active power curves, and Fig. 15b shows ISE and THD performance for different PI controller settings from the indicated τ_i parameter. The simulated results suggest that lower τ_i values produce better dynamic performance, decreasing overshoot up to 3% and settling time up to 0.8 ms for $\tau_i = 0.053$ ms, close to the 0.05 ms threshold [39]. Fig. 15b corroborates the tendency for improved system performance with decreasing, indicating $\tau_i = 0.053\ ms$ as the best setting for the PI controller, with gains $k_p = 1.5238$ and $k_i = 0.0952$ and discrete transfer function shown in (19). The PI-DPC control in (19) resulted in a phase margin of 58° and gain margin of 3.22 dB [7]. Fig. 16 shows the test results for the PI DPC and Table 3 and Fig. 17 summarizes the comparison with the best fit MPC-DPC designed here (Fig. 12).

$$C(z) = \frac{1.5238\,(z - 0.9375)}{z - 1} \tag{19}$$

Note that the ISE and THD values in Table 3 show a better performance of the controller proposed here over the PI DPC, both in power regulation and energy quality. The controller proposed here also performed better in the transient regime with $t_s = 0.86$ ms and no overshoot (Fig. 17a), while the PI controller has an overshoot of 4% and $t_s = 1.7$ ms. In the current spectrum for the PI-DPC controller

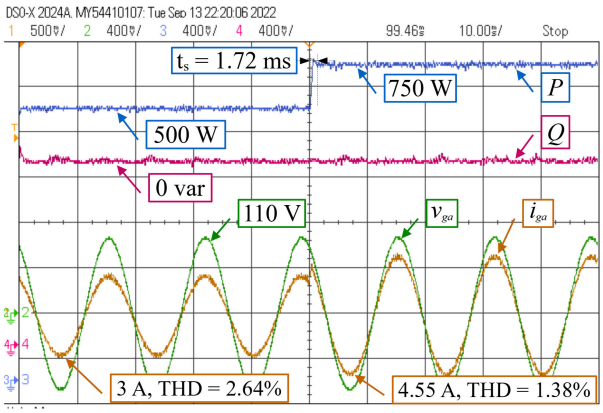

FIGURE 16. Experimental power regulation for the PI-DPC.

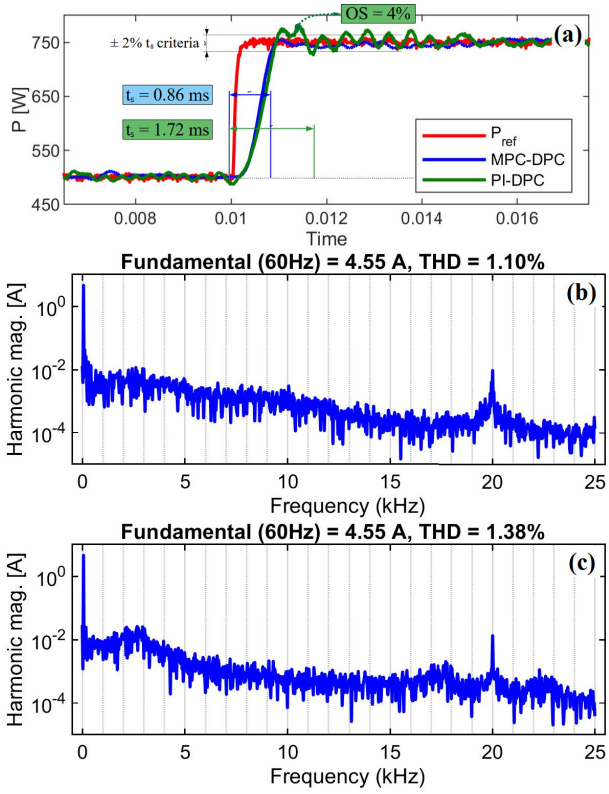

FIGURE 17. Comparison between the MPC-DPC and the PI DPC: (a) Active Power Transient; (b) MPC - Amplitude spectrum of $i_{g,a}$ in Fig. 12; (c) PI - Amplitude spectrum of $i_{g,a}$ in Fig. 16.

(Fig. 17c), the higher amplitude of harmonic components in the 2-3 kHz and 16-17 kHz bands may contribute to the worse performance compared to the MPC-DPC controller proposed here (Fig. 17b).

It is important to emphasize that the PI controller is not optimized to reduce the control effort as well as the MPC-DPC [9], as shown in Fig. 18 the comparison of the control signal (vector norm of (15)) for the same boundary conditions and reference signals used for Fig. 4. In Fig. 18, the maximum control signal levels of 32.9 Vrms for the MPC-DPC, while

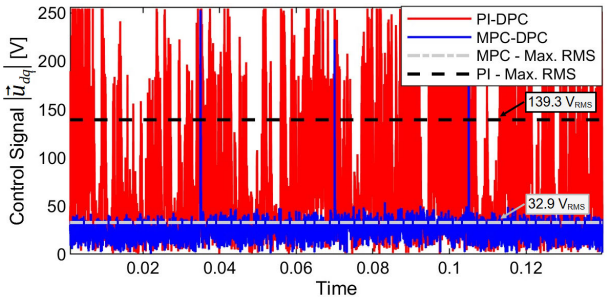

FIGURE 18. Comparison of the PI and MPC control signals for the same boundary conditions and reference signals used for Fig. 4.

the PI controller produced signals up to 139.3 Vrms. The MPC control effort is less than a quarter of the PI controller (Fig. 18), which may be one of the reasons for the better performance in power regulation (Table 3). In addition, the MPC presents other features, such as being more closely related to the plant dynamics and based on the future behavior prediction [12].

VI. CONCLUSION

In this paper, we designed an MPC-DPC controller with PWM modulation in the synchronous rotating frame for a grid-connected VSC with L-filter. We proposed an initial control setting based on the VSC nominal setup to guarantee stability. The coarse tuning of the MPC-DPC controller was developed from the theoretical dynamic performance given by the closed-loop poles of the control system. Fine-tuning can be identified visually using the performance maps built from simulations that sweep the weight factors of the cost function and the time horizons of the predictive model. In the present literature, no reports have been found on such detailed analyses of the performance of the MPC-DPC controller applied to grid-connected VSCs. The proposed settings for the control system were validated experimentally on a low-power experimental bench.

The overall performance of the MPC-DPC was proven to enhance when reducing the ratio of the cost function weight factors from the stability threshold $\gamma_u/\gamma_y = 10^2$ to the minimum threshold $\gamma_u/\gamma_y > 10^{-1}$, imposed by the saturation of the PWM modulator. The analyses showed that the setting $\gamma_u/\gamma_y \approx 10^{-1}$, whatever the individual values of γ_y or γ_u and whatever the time horizons, can guarantee good performance for the grid-connected VSC in transitory, in power regulation and energy quality. Compared with the PI-DPC controller, the proposed tuning for the MPC-DPC controller outperformed both power regulation and energy quality and only required a quarter of the control effort of the PI controller.

REFERENCES

[1] V. Masson-Delmotte et al., "Climate change 2021: The physical science basis. Contribution of working group I to the sixth assessment report of the intergovernmental panel on climate change," 2021, vol. 2.

[2] T. Dragicevic, S. Vazquez, and P. Wheeler, "Advanced control methods for power converters in DG systems and microgrids," *IEEE Trans. Ind. Electron.*, vol. 68, no. 7, pp. 5847–5862, Jul. 2021.

[3] L. Meegahapola, A. Sguarezi, J. S. Bryant, M. Gu, D. E. R. Conde, and R. B. A. Cunha, "Power system stability with power-electronic converter interfaced renewable power generation: Present issues and future trends," *Energies*, vol. 13, no. 13, p. 3441, Jul. 2020.

[4] X. Chen, W. Wu, N. Gao, H. S.-H. Chung, M. Liserre, and F. Blaabjerg, "Finite control set model predictive control for LCL-filtered grid-tied inverter with minimum sensors," *IEEE Trans. Ind. Electron.*, vol. 67, no. 12, pp. 9980–9990, Dec. 2020.

[5] R. N. Beres, X. Wang, M. Liserre, F. Blaabjerg, and C. L. Bak, "A review of passive power filters for three-phase grid-connected voltage-source converters," *IEEE Trans. J. Emerg. Sel. Topics Power Electron.*, vol. 4, no. 1, pp. 54–69, Mar. 2016.

[6] C. Xie, K. Li, J. Zou, D. Liu, and J. M. Guerrero, "Passivity-based design of grid-side current-controlled *LCL*-type grid-connected inverters," *IEEE Trans. Power Electron.*, vol. 35, no. 9, pp. 9813–9823, Sep. 2020.

[7] Y. Gui, X. Wang, F. Blaabjerg, and D. Pan, "Control of grid-connected voltage-source converters: The relationship between direct-power control and vector-current control," *IEEE Ind. Electron. Mag.*, vol. 13, no. 2, pp. 31–40, Jun. 2019.

[8] W. Taha, A. R. Beig, and I. Boiko, "Quasi optimum PI controller tuning rules for a grid-connected three phase AC to DC PWM rectifier," *Int. J. Electr. Power Energy Syst.*, vol. 96, pp. 74–85, Mar. 2018.

[9] Y. Wu, X. Zhao, K. Li, M. Zheng, and S. Li, "Energy saving—Another perspective for parameter optimization of P and PI controllers," *Neurocomputing*, vol. 174, pp. 500–513, Jan. 2016.

[10] D. Perez-Estevez, J. Doval-Gandoy, A. G. Yepes, O. Lopez, and F. Baneira, "Generalized multifrequency current controller for grid-connected converters with LCL filter," *IEEE Trans. Ind. Appl.*, vol. 54, no. 5, pp. 4537–4553, Sep. 2018.

[11] J. Rodriguez and P. Cortes, *Predictive Control of Power Converters and Electrical Drives*. Hoboken, NJ, USA: Wiley, 2012.

[12] A. J. S. Filho, *Model Predictive Control for Doubly-Fed Induction Generators and Three-Phase Power Converters*. Amsterdam, The Netherlands: Elsevier, 2022.

[13] C. Bordons, F. Garcia-Torres, and M. A. Ridao, *Model Predictive Control of Microgrids*. Cham, Switzerland: Springer, 2020.

[14] J. Rossiter, *Model-Based Predictive Control: A Practical Approach* (Control Series). Boca Raton, FL, USA: CRC Press, 2003.

[15] J. A. Rossiter, *Model-Based Predictive Control*, J. Rossiter, Ed. Boca Raton, FL, USA: CRC Press, Jul. 2017.

[16] L. Chen, H. Nian, and Y. Xu, "Improved model predictive direct power control of grid side converter in weak grid using Kalman filter and DSOGI," *Chin. J. Electr. Eng.*, vol. 5, no. 4, pp. 22–32, Dec. 2019.

[17] Y. Gui, C. Kim, C. C. Chung, J. M. Guerrero, Y. Guan, and J. C. Vasquez, "Improved direct power control for grid-connected voltage source converters," *IEEE Trans. Ind. Electron.*, vol. 65, no. 10, pp. 8041–8051, Oct. 2018.

[18] A. J. S. Filho and E. R. Filho, "Model-based predictive control applied to the doubly-fed induction generator direct power control," *IEEE Trans. Sustain. Energy*, vol. 3, no. 3, pp. 398–406, Jul. 2012.

[19] A. S. Lunardi, A. J. S. Filho, C. E. Capovilla, I. R. S. Casella, and A. A. M. de Medeiros, "A wireless coded predictive direct power control for renewable energy sources in smart grid environment," *Int. J. Electr. Power Energy Syst.*, vol. 112, pp. 319–325, Nov. 2019.

[20] R. Panigrahi, S. K. Mishra, S. C. Srivastava, A. K. Srivastava, and N. N. Schulz, "Grid integration of small-scale photovoltaic systems in secondary distribution network—A review," *IEEE Trans. Ind. Appl.*, vol. 56, no. 3, pp. 3178–3195, May 2020.

[21] X. Zhang, D. Xia, Z. Fu, G. Wang, and D. Xu, "An improved feedforward control method considering PLL dynamics to improve weak grid stability of grid-connected inverters," *IEEE Trans. Ind. Appl.*, vol. 54, no. 5, pp. 5143–5151, Sep./Oct. 2018.

[22] A. Lunardi, E. R. Conde D, J. de Assis, D. A. Fernandes, and A. J. S. Filho, "Model predictive control with modulator applied to grid inverter under voltage distorted," *Energies*, vol. 14, no. 16, p. 4953, Aug. 2021.

[23] L. L. Rodrigues, O. A. C. Vilcanqui, A. L. L. F. Murari, and A. J. S. Filho, "Predictive power control for DFIG: A FARE-based weighting matrices approach," *IEEE J. Emerg. Sel. Topics Power Electron.*, vol. 7, no. 2, pp. 967–975, Jun. 2019.

[24] J. Liu, Y. Miura, and T. Ise, "Cost-function-based microgrid decentralized control of unbalance and harmonics for simultaneous bus voltage compensation and current sharing," *IEEE Trans. Power Electron.*, vol. 34, no. 8, pp. 7397–7410, Aug. 2019.

[25] J. Hu, Y. Shan, J. M. Guerrero, A. Ioinovici, K. W. Chan, and J. Rodriguez, "Model predictive control of microgrids—An overview," *Renew. Sustain. Energy Rev.*, vol. 136, Feb. 2021, Art. no. 110422.

[26] N. Vázquez and J. V. López, "Inverters," in *Power Electronics Handbook*. Amsterdam, The Netherlands: Elsevier, 2018, pp. 289–338.

[27] A. J. S. Filho, M. E. de Oliveira Filho, and E. R. Filho, "A predictive power control for wind energy," *IEEE Trans. Sustain. Energy*, vol. 2, no. 1, pp. 97–105, Jan. 2011.

[28] G. Abad, J. Lopez, M. Rodriguez, L. Marroyo, and G. Iwanski, *Doubly Fed Induction Machine: Modeling and Control for Wind Energy Generation Applications*, M. E. El-Hawary, Ed. Hoboken, NJ, USA: Wiley, 2011.

[29] L. Zhao, W. Song, and Z. Ruan, "Discrete domain design scheme of complex-vector current controller for induction motor at low switching frequency," *IEEE Trans. Transport. Electrific.*, early access, Jun. 23, 2022, doi: 10.1109/TTE.2022.3185789.

[30] H. Tu, H. Feng, S. Srdic, and S. Lukic, "Extreme fast charging of electric vehicles: A technology overview," *IEEE Trans. Transport. Electrific.*, vol. 5, no. 4, pp. 861–878, Dec. 2019.

[31] M. G. Judewicz, S. A. González, J. R. Fischer, J. F. Martínez, and D. O. Carrica, "Inverter-side current control of grid-connected voltage source inverters with LCL filter based on generalized predictive control," *IEEE J. Emerg. Sel. Topics Power Electron.*, vol. 6, no. 4, pp. 1732–1743, Dec. 2018.

[32] G. F. Franklin, J. D. Powell, A. Emami-Naeini, and J. D. Powell, *Feedback Control of Dynamic Systems*, vol. 4. Upper Saddle River, NJ, USA: Prentice-Hall, 2002.

[33] R. Guzman, L. G. de Vicuna, A. Camacho, J. Miret, and J. M. Rey, "Receding-horizon model-predictive control for a three-phase VSI with an *LCL* filter," *IEEE Trans. Ind. Electron.*, vol. 66, no. 9, pp. 6671–6680, Sep. 2019.

[34] S. Skogestad and I. Postlethwaite, *Multivariable Feedback Control: Analysis and Design*. Hoboken, NJ, USA: Wiley, 2005.

[35] L. A. Maccari, D. M. Lima, G. G. Koch, and V. F. Montagner, "Robust model predictive controller applied to three-phase grid-connected LCL filters," *J. Control, Autom. Electr. Syst.*, vol. 31, no. 2, pp. 447–460, Apr. 2020.

[36] H. S. Das, M. M. Rahman, S. Li, and C. W. Tan, "Electric vehicles standards, charging infrastructure, and impact on grid integration: A technological review," *Renew. Sustain. Energy Rev.*, vol. 120, Mar. 2020, Art. no. 109618.

[37] C. Alfaro, R. Guzman, L. G. D. Vicuña, J. Miret, and M. Castilla, "Dual-loop continuous control set model-predictive control for a three-phase unity power factor rectifier," *IEEE Trans. Power Electron.*, vol. 37, no. 2, pp. 1447–1460, Feb. 2022.

[38] D. Pérez-Estévez and J. Doval-Gandoy, "A finite-control-set linear current controller with fast transient response and low switching frequency for grid-tied inverters," *IEEE Trans. Ind. Appl.*, vol. 56, no. 6, pp. 6546–6564, Nov. 2020.

[39] M. Yazdanian and A. Mehrizi-Sani, "Internal model-based current control of the *RL* filter-based voltage-sourced converter," *IEEE Trans. Energy Convers.*, vol. 29, no. 4, pp. 873–881, Dec. 2014.

JEFFERSON S. COSTA received the B.S. and M.S. degrees in electrical engineering from the Federal University of Pará (UFPA), Tucuruí, Pará, Brazil, in 2013 and 2016, respectively. He is currently pursuing the Ph.D. degree in energy with the Federal University of ABC (UFABC), Santo André, Brazil. From 2014 to 2016, he collaborated with the Physics Department, Pontificia Universidade Católica do Rio de Janeiro (PUC-Rio), Rio de Janeiro, Brazil, where he worked on the development of photonic nanosensors. He is currently a Professor at UFPA, teaching calculus, electromagnetism, and electrical materials. His research interests include control applied to machine drives, power converters, electric vehicles, and photovoltaic and wind energy.

ANGELO LUNARDI received the degree in electronic engineering from the Instituto Mauá Tecnologia, in 2015, the master's degree in electrical engineering from the Universidade Federal do ABC (UFABC), with a focus on control research applied to wind power generation, in 2017, and the Ph.D. degree in electrical engineering from the University of São Paulo (USP) with a thesis titled robust predictive control applied to the converter connected to the grid, in 2022. Currently, he is a Researcher with the UFABC and works with control systems for renewable energy.

POLLYANA C. RIBEIRO received the B.S. degree in material science engineering from the Federal University of Paraiba, Brazil, in 2005, and the M.S. and Ph.D. degrees from the Federal University of Campina Grande, Brazil, in 2007 and 2011, respectively. She is currently an Associate Professor with the Department of Renewable Energy Engineering, Federal University of Paraiba. She was a Visiting Scholar at the Virginia Polytechnic Institute and State University (Virginia Tech), Blacksburg, USA, from 2018 to 2019. Her current research interest includes electrical characterization of photovoltaic cells.

IAGO B. DA SILVA received the B.S. degree in renewable energy engineering from the Federal University of Paraiba, Brazil, in 2021, where he is currently pursuing the M.S. degree in renewable energy engineering. His research interest includes the electrical characterization of photovoltaic cells.

DARLAN ALEXANDRIA FERNANDES (Member, IEEE) received the B.S. degree in electrical engineering from the Federal University of Paraiba, Brazil, in 2002, and the M.S. and Ph.D. degrees in electrical engineering from the Federal University of Campina Grande, Brazil, in 2004 and 2008, respectively. He was a Visiting Scholar at the Center for Power Electronics Systems (CPES), Virginia Polytechnic Institute and State University (Virginia Tech), Blacksburg, USA, from 2018 to 2019. From 2007 to 2011, he was a Professor with the Federal Center of Technological Education of Rio Grande do Norte, Industry Department. He is currently an Assistant Professor with the Department of Electrical Engineering, Federal University of Paraiba. His research interests include the applications of power electronics in distribution systems, power quality, photovoltaic systems, and impedance-based control design techniques for static converters.

ALFEU J. SGUAREZI FILHO (Senior Member, IEEE) received the master's and Ph.D. degrees in electrical engineering from the Faculty of Electrical and Computer Engineering, University of Campinas (UNICAMP), in 2007 and 2010, respectively. Currently, he is an Associate Professor at the Federal University of ABC (UFABC). He is the author of several articles in national and international scientific journals and book chapters in the areas of electrical machines, machine drives, electric vehicles, power electronics, and wind and photovoltaic energies.